

Boosting the Edelstein effect of two-dimensional electron gases by ferromagnetic exchange

Gabriel Lazrak,¹ B3rge G3bel,² Agn3s Barth3l3my,¹ Ingrid Mertig,² Annika Johansson,^{3,*} and Manuel Bibes^{1,†}

¹*Unit3e Mixte de Physique, CNRS, Thales, Universit3e Paris-Saclay, 91767, Palaiseau, France*

²*Institut f3ur Physik, Martin-Luther-Universit3t, Halle-Wittenberg, 06099 Halle (Saale), Germany*

³*Max Planck Institute of Microstructure Physics, Weinberg 2, 06120 Halle (Saale), Germany*

(Dated: October 6, 2023)

Strontium titanate (SrTiO₃) two-dimensional electron gases (2DEGs) have broken spatial inversion symmetry and possess a finite Rashba spin-orbit coupling. This enables the interconversion of charge and spin currents through the direct and inverse Edelstein effects, with record efficiencies at low temperature, but more modest effects at room temperature. Here, we show that making these 2DEGs ferromagnetic enhances the conversion efficiency by nearly one order of magnitude. Starting from the experimental band structure of non-magnetic SrTiO₃ 2DEGs, we mimic magnetic exchange coupling by introducing an out-of-plane Zeeman term in a tight-binding model. We then calculate the band structure and spin textures for increasing internal magnetic fields and compute the Edelstein effect using a semiclassical Boltzmann approach. We find that the conversion efficiency first increases strongly with increasing magnetic field, then shows a maximum and finally decreases. This field dependence is caused by the competition of the exchange coupling with the effective Rashba interaction. While enhancing the splitting of band pairs amplifies the Edelstein effect, weakening the in-plane Rashba-type spin texture reduces it.

I. INTRODUCTION

Since the discovery of a quasi-two-dimensional electron gas (2DEG) at the interface between the two band insulators LaAlO₃ and SrTiO₃ (STO) [1], 2DEGs at oxide surfaces and interfaces have attracted a lot of attention due to their very rich physics. Superconductivity [2], magnetism [3, 4], gate tunable metal-insulator and superconductor-insulator transitions [5, 6] as well as Rashba spin-orbit coupling [7] make them also promising for applications [8, 9]. Additionally, recent experiments have revealed their unprecedented efficiency for spin to charge current interconversion [10, 11], which is key for new devices such as the magneto-electric spin transistor proposed by Intel for beyond CMOS computing schemes [12]. As described in more detail in Refs. [10, 11], in those 2DEGs, the inversion symmetry breaking at the interface results in a built-in electric field perpendicular to the interface and thus an additional effective term in the Hamiltonian of the system, the Rashba term, that lifts the spin degeneracy and locks the spin and momentum degrees of freedom. In the simplest case of linear Rashba coupling, this results in two slightly different Fermi contours with opposite spin chiralities. In the inverse Edelstein effect, the injection of a pure spin current perpendicular to the interface can be interpreted as a shift of the two contours in opposite directions to accommodate the spin accumulation. This slight non-equivalence leads to the generation of a charge current within the 2DEG (spin-charge conversion). Its reciprocal effect, the direct Edelstein effect, is achieved by applying an electric field

that leads to a reoccupation of states, often visualized as a shift of both Fermi contours in the same direction. This results in a net spin density generation that can diffuse as a pure spin current into an adjacent material (charge-spin conversion).

Recently, possibilities to further enlarge or control the functionalities of STO 2DEGs have emerged. One approach relies on making the 2DEG ferroelectric by exploiting the large electric-field- or Ca-doping-induced ferroelectric character in STO [13, 14], thereby enabling a non-volatile control of the transport and spin-charge interconversion properties. Another is by inducing spin polarization in the 2DEG by depositing a magnetic layer on top of STO [15–21]. Combining both strategies, multiferroic 2DEGs have been realized [22], opening an avenue for ferroelectrically controllable chiral spin textures in 2DEGs and providing a new playground for non-volatile spin-orbitronics and non-reciprocal physics.

Here, by combining a tight-binding Hamiltonian and a semiclassical Boltzmann approach, we predict that introducing ferromagnetism in STO 2DEGs can enhance the spin-charge interconversion efficiency by nearly one order of magnitude. The non-monotonic dependence of this efficiency with the amplitude of the induced magnetization is explained by the interplay between magnetic exchange coupling and Rashba-like spin-orbit coupling, that causes a sub-band splitting, as well as a magnetically induced out-of-plane spin polarization. This enhancement is of great promise to obtain spin-charge interconversion large enough for room temperature applications.

II. BAND STRUCTURE AND SPIN TEXTURE

We use an effective eight-band tight-binding model introduced in Refs. [11, 23–25] in order to model the t_{2g}

* annika.johansson@mpi-halle.mpg.de

† manuel.bibes@cnrs-thales.fr

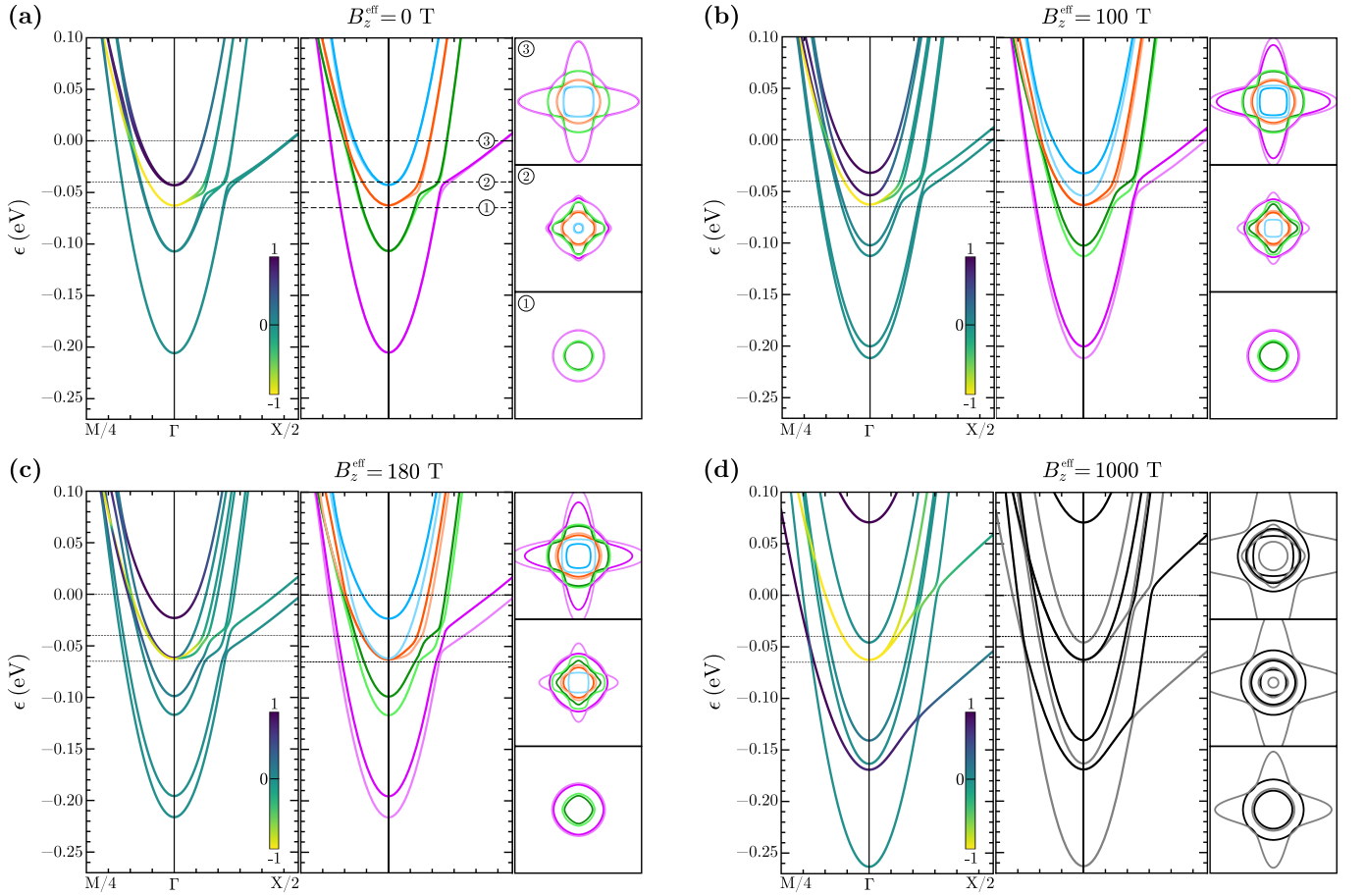


FIG. 1. **Band structure and iso-energy lines of the 2DEG at STO interfaces.** The band structure is computed using the tight-binding model introduced in the Appendix A, for four exchange field strengths ($B_z^{\text{eff}} = 0$ T (a), 100 T (b), 180 T (c), and 1000 T (d)). The middle graph of each panel displays the band structure using four colors (magenta, green, orange, blue), with the lower energy bands shown in lighter shades and the higher energy bands shown in darker shades for each pair. On the right, the Fermi lines (with $|k_x|, |k_y| \leq \pi/2a$) illustrate the splitting of the bands for three specific energies (0 meV, -40 meV, and -65 meV in that order). The expectation value of the operator $\mathcal{L}_z \mathcal{S}_z$ (normalized to $\hbar^2/2$) is depicted on the left. For panel (d), the band structure and Fermi contours are displayed in black and gray due to significant intertwining of the bands, making it unreasonable to group them by pairs.

electronic states which are relevant for the formation of the 2DEG at STO interfaces. Our model includes two d_{xy} orbitals as well as one d_{yz} and one d_{zx} orbital and has been demonstrated to appropriately approximate the electronic structure of the 2DEG at the STO surface, as well as the interface with LaAlO_3 and AlO_x [11, 25]. For details of this model, we refer to Refs. [11, 26] and to Appendix A. In addition to atomic spin-orbit coupling, the broken inversion symmetry at the interface allows for an inter-atomic orbital mixing term, which leads to an effective Rashba term causing a Rashba-like spin splitting of the bands [23, 24]. In order to simulate ferromagnetism originating from an adjacent ferromagnetic layer, we introduce an additional magnetic exchange coupling term to the Hamiltonian, $\mathcal{H} = \mathcal{H}_{\text{STO}} + \mathcal{H}_{\text{ex}}$, with \mathcal{H}_{STO} the Hamiltonian of the unperturbed STO interface, and the

exchange coupling

$$\mathcal{H}_{\text{ex}} = -\frac{J_{\text{ex}}}{\hbar} (g_l \mathcal{L} + g_s \mathcal{S}) \cdot \hat{\mathbf{M}} \quad (1)$$

Here, \hbar is the reduced Planck constant, $\hat{\mathbf{M}}$ is the direction of the magnetization, J_{ex} quantifies the exchange coupling between the conduction electrons' orbital/spin moments and the magnetization, \mathcal{L} and \mathcal{S} are the operators of the orbital angular momentum and the spin, respectively, with g_l and g_s the corresponding Landé factors. The Hamiltonian (1) has the form of a Zeeman Hamiltonian [27]

$$\mathcal{H}_{\text{ex}} \hat{=} \mathcal{H}_Z = \frac{\mu_B}{\hbar} (g_l \mathcal{L} + g_s \mathcal{S}) \cdot \mathbf{B}^{\text{eff}} \quad (2)$$

with μ_B the Bohr magneton and $\mathbf{B}^{\text{eff}} = -J_{\text{ex}} \hat{\mathbf{M}} / \mu_B$ an effective magnetic field originating from the finite magnetization and acting on the electronic states. The Landé

factors are assumed $g_l = 1$ and $g_s = 2$, following Ref. [26]. A representation of the spin and orbital moment operators in the basis of the relevant t_{2g} orbitals can be found in Eqs. (A5)-(A7).

In the following, the influence of magnetic exchange coupling on the band structure as well as the charge-spin conversion efficiency are discussed in terms of the effective magnetic field \mathbf{B}^{eff} . Importantly, this field, originating from magnetic exchange interaction, can induce energy splitting in the band structure of a few 10 meV [28], which corresponds to a B^{eff} of a few hundred Tesla. Therefore, the magnetic field B^{eff} discussed in the following is much larger than external magnetic fields which can be applied experimentally but could correspond to the field induced by a magnetic exchange interaction in the 2DEG.

First, we examine the electronic band structure of the 2DEG at STO interfaces under the influence of an out-of-plane magnetic exchange field, using the model Hamiltonian introduced in Eq. (1). Figure 1 illustrates the band structure at four different out-of-plane exchange field strengths ($B_z^{\text{eff}} = 0\text{ T}, 100\text{ T}, 180\text{ T},$ and 1000 T) within an energy range of -270 meV to 100 meV . For each exchange field strength, the band structure as well as iso-energy lines at three selected energies (-65 meV , -40 meV , and 0 meV) are shown to illustrate the influence of the exchange field on the band structure.

At zero field (Figure 1a), the splitting of each band pair (marked magenta, green, orange, and blue in the right panel) is solely due to the atomic spin-orbit coupling and antisymmetric hopping (called orbital mixing in Refs. [11, 25]), which lift the twofold spin degeneracy. Close to the band edge of each band pair, the band structure is isotropic with circular iso-energy lines (① in the figure). The heavy bands' Fermi contours take the form of two perpendicular ellipses. The maximum splittings along ΓX are observed in the region from -65 meV to -40 meV , where avoided crossings occur, the first one between the green and orange band pairs and the second one between the magenta and green band pairs, as highlighted by the Fermi surface at -40 meV (② in the figure). In these regions, we observe a strong deviation from the simple Rashba model for free electrons.

Upon increasing the exchange field strength, we observe the expected linear increase of Zeeman-like splitting for each band pair, with the notable exception of the orange band pair that remains unsplit at Γ . To understand this band-dependent splitting caused by the exchange field, it is crucial to analyze the spin and orbital composition of the bands. By breaking the inversion symmetry at the (001) interface, the t_{2g} bands become inequivalent in energy which is why the d_{xy} bands appear at a lower energy near the Γ point compared to the d_{yz} and d_{xz} bands. Due to SOC, states that are close in energy hybridize. In our case, the d_{yz} and d_{xz} states form the superpositions $d_{m_l=\pm 1} = (-id_{yz} \mp d_{xz})/\sqrt{2}$, meaning that the cubic atomic orbitals d_{yz} , d_{xz} form the atomic orbitals $d_{m_l=\pm 1}$. They are characterized by the quantum

numbers $l = 2, m_l = \pm 1$, with l the orbital angular momentum quantum number, and m_l the quantum number of the out-of-plane orbital angular momentum operator.

The magnetic exchange field couples with both orbital angular momentum and spin, see Eq. (1). States with purely d_{xy} , d_{yz} , or d_{zx} character exhibit zero orbital angular momentum. However, since the t_{2g} orbitals hybridize they may possess nonzero expectation values of the out-of-plane orbital angular momentum $L_z = \hbar m_l$, because $m_l \neq 0$ as explained above. The left panel of each subfigure of Fig. 1 illustrates the spin and orbital character of the electronic states. Here, we show the expectation value of the product of out-of-plane orbital and spin operators, $\mathcal{L}_z \mathcal{S}_z$. On the colorbar: '1' means that the corresponding eigenvalues have the same sign (e.g. $m_l = 1, m_s = 1/2$, the parallel state), '-1' means opposite sign (e.g. $m_l = 1, m_s = -1/2$, the antiparallel state) and '0' means zero out-of-plane orbital quantum number (e.g. $m_l = 0$).

In the third lowest band pair (orange) spin and orbital angular momenta are antiparallel because the eigenstates are superpositions of states with opposite signs of the quantum numbers m_l and m_s ($d_{m_l=-1, m_s=1/2}$ and $d_{m_l=1, m_s=-1/2}$). In the fourth band pair (blue), they are parallel (superpositions of states with the same sign of m_l and m_s : $d_{m_l=1, m_s=1/2}$ and $d_{m_l=-1, m_s=-1/2}$). When a magnetic field is applied, the bands are polarized with respect to spin and orbital momenta. Due to the quantum numbers discussed above, the effects of the orbital- and spin-induced band splitting are compensated for the orange band pair $\Delta\epsilon = 2\mu_B(g_l\Delta L_z + g_s\Delta S_z)/\hbar \approx 0$ because $\Delta L_z \approx -2\Delta S_z$ and $g_s = 2g_l$, but are enhanced in the blue band pair $\Delta\epsilon = 2\mu_B(g_l\Delta L_z + g_s\Delta S_z)/\hbar \approx 4\mu_B|\mathbf{B}^{\text{eff}}|$.

Since the lower two band pairs (magenta and green) consist of almost purely d_{xy} states at the Γ point at low magnetic fields, the orbital angular momentum L_z is suppressed for these bands which is why they only split up due to the spin contribution: $\Delta\epsilon = 2\mu_B g_s \Delta S_z / \hbar \approx 2\mu_B |\mathbf{B}^{\text{eff}}|$. These bands could only experience a considerable orbital polarization if they hybridized (a) with the orange and blue bands or (b) with $d_{x^2-y^2}$ states to form the complex orbitals $d_{m_l=\pm 2} = (d_{x^2-y^2} \pm id_{xy})/\sqrt{2}$ that are characterized by $m_l = \pm 2$.

At specific field strengths, the Zeeman-like splitting causes band crossings at Γ . This leads to increased band mixing, making it unreasonable to discuss them as pairs. At 180 T, the first such crossing occurs between the orange bands and lower blue band. We will explore the implications of this crossing on the spin-charge interconversion efficiency later. Thus, the center panel of Figure 1d is displayed in black and gray to prevent any potential confusion regarding the concept of a band pair and its associated color representation.

To further highlight the impact of the exchange field, the spin textures at various field strengths, corresponding to the iso-energy contours depicted in Figure 1, are presented in Figure 2. When no out-of-plane exchange field is present (Fig. 2a), the spins are oriented within

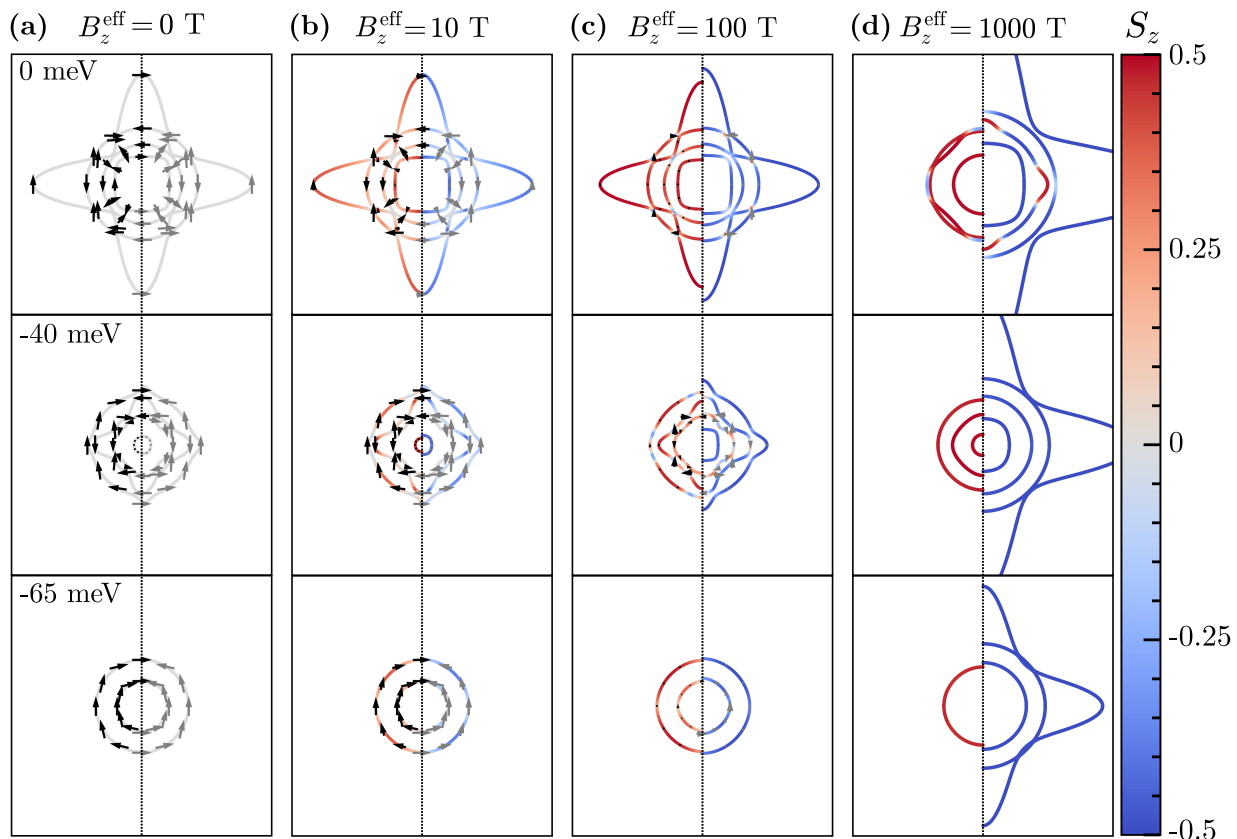


FIG. 2. **Iso-energy lines and spin textures.** The contour energies are the same as in Fig.1 (0 meV, -40 meV, and -65 meV in that order). The exchange field strengths are different ($B_z^{\text{eff}} = 0$ T (a), 10 T (b), 100 T (c), and 1000 T (d)). The arrows represent the in-plane spin expectation values, while the color indicates the out-of-plane spin expectation values. For better visibility, the left and right sides of each figure correspond to the higher energy band and lower energy band of a pair, respectively, except for 1000 T, where it corresponds to positive (resp. negative) values of S_z at Γ .

the plane, resulting in a zero out-of-plane spin density. The arrows in the figure, representing the in-plane spins, exhibit the familiar Rashba texture for circular contours, with the absolute values of the spin expectation values equal to $\hbar/2$. At higher energies, the spin texture becomes more intricate notably at avoided crossing points [11].

As the magnetic exchange field is increased, the in-plane spin expectation values diminish notably in favor of increased out-of-plane spin expectation values giving rise to an out-of-plane equilibrium spin magnetization of the 2DEG. This change of orientation is particularly pronounced, with the absolute out-of-plane spin expectation values (represented by the color) close to $\hbar/2$ at 1000 T (Fig. 2d). More importantly, this spin reorientation would lead to a reduction of the current-induced non-equilibrium in-plane spin polarization by the Edelstein effect and to a reduction of the produced charge current by the inverse Edelstein effect when spin current is injected. Figure 2 also evidences the large impact of the field-induced Zeeman-like splitting on the bands present at the different energies and the potential of this out-of-plane field to reinforce the contrast between contours

with opposite spin chiralities and thus to boost the spin-charge interconversion. The effective impact of those two counteracting effects on spin-charge interconversion is described in the next section.

III. EDELSTEIN EFFECT

The spin Edelstein effect, which is the main focus of this work, corresponds to a non-equilibrium spin density, leading to a finite magnetization, induced by an external electric field. In order to quantify this effect, we define the spin Edelstein susceptibility χ^s ,

$$\mathbf{m} = \mathbf{m}_0 + \chi^s \mathbf{E} \quad (3)$$

with \mathbf{m} the total magnetic moment per unit cell, \mathbf{m}_0 the equilibrium magnetic moment per unit cell, and $\chi^s \mathbf{E}$ the magnetic moment originating from the current-induced spin density. The rank-2 tensor χ^s is the spin Edelstein susceptibility, and \mathbf{E} is the external electric field (producing the current). However, in addition to this spin Edelstein effect (SEE), the electrons' orbital magnetic moments can also give rise to a finite current-induced

magnetization, called orbital Edelstein effect (OEE) [29–34]. It has been shown that at STO interfaces, the OEE can exceed the SEE remarkably [26]. However, given that the experimental realization of the Edelstein effect typically observes only the SEE [11, 26, 35, 36], our work focuses only on the SEE.

Within the semiclassical Boltzmann transport theory, the spin Edelstein susceptibility defined by Eq. (3) is given by

$$\chi_{ij}^s = g_s \frac{A_0 e \mu_B}{A \hbar} \sum_{\mathbf{k}} \tau_{\mathbf{k}} \mathbf{S}_{\mathbf{k}}^i \mathbf{v}_{\mathbf{k}}^j \delta(\epsilon_{\mathbf{k}} - \epsilon_F). \quad (4)$$

Here, A_0 is the area of the unit cell, A is the area of the sample, e is the absolute value of the elementary charge, the multi-index \mathbf{k} represents the crystal momentum of an electronic state $|\mathbf{k}\rangle$ as well as the band index, $\tau_{\mathbf{k}}$ is the momentum relaxation time, which is set constant $\tau_{\mathbf{k}} = \tau_0$ in the following, $\mathbf{S}_{\mathbf{k}}$ is the spin expectation value of the state $|\mathbf{k}\rangle$, $\mathbf{v}_{\mathbf{k}}$ is the group velocity, $\epsilon_{\mathbf{k}}$ is the energy of the state $|\mathbf{k}\rangle$, and ϵ_F is the Fermi energy. We have used the relaxation time approximation to solve the linearized Boltzmann equation and assumed zero temperature. Details of the Boltzmann transport theory can be found in Appendix B.

The symmetry of the system allows for nonzero tensor elements $\chi_{xy}^s = -\chi_{yx}^s$, which quantify a current-induced magnetization oriented perpendicular to the applied electric field. In the presence of a nonzero magnetic exchange field, the current-induced magnetization can also exhibit a component parallel to \mathbf{E} due to the broken time-reversal symmetry, represented by $\chi_{xx}^s = \chi_{yy}^s$. However, in the system under consideration, the extrinsic Edelstein effect, calculated within the Boltzmann approach, does not provide any contribution to χ_{xx}^s . This tensor element can be nonzero only due to the intrinsic Edelstein effect, calculated for example using the Kubo approach. As shown in Refs.[37, 38], for a pure Rashba system with Zeeman-like splitting these intrinsic contributions to the current-induced magnetization are several orders of magnitude smaller than the extrinsic contributions as well as the equilibrium magnetization. Therefore, they are not discussed in this work.

Figure 3 illustrates the SEE conversion efficiency as a function of the Fermi level at various exchange field strengths. The efficiency at $B_z^{\text{eff}} = 0$ T is depicted in red. It exhibits two positive maxima at -65 meV and -15 meV and a negative maximum around -50 meV. The introduction of an out-of-plane exchange field notably enhances this efficiency around -65 meV, by approximately an order of magnitude at 180 T; beyond this value the efficiency gradually decreases. A similar trend is observed in the -50 meV to -40 meV region, albeit with a negative efficiency, but the maximum is attained at a lower field (approximately 70 T). These findings highlight the significant impact of the exchange field on the SEE conversion efficiency and provide crucial insights into its optimal operating conditions. By fine-tuning

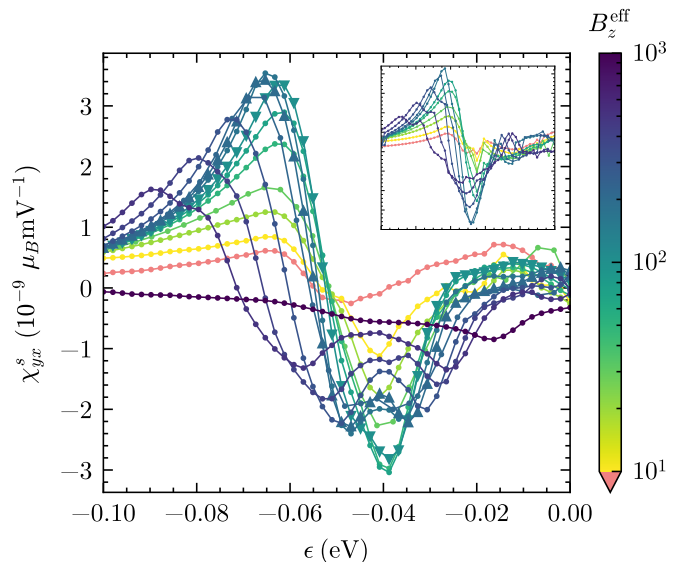


FIG. 3. **Spin Edelstein effect conversion efficiency as a function of the energy at various exchange field strengths.** The exchange field strengths range from 0 T to 1000 T and the energy ranges from -100 meV to 0 meV. The conversion efficiency at zero field is represented in red. To compare with previous figures, the downward (resp. upward)-pointing triangles represent 100 T (resp. 180 T). The inset corresponds to the product of average wave vector k and the average modulus of the in-plane spin expectation value of each band; for details see main text.

both B_z^{eff} and ϵ_F , a strong increase of the SEE in STO-based 2DEGs can be achieved.

To understand the strong B_z^{eff} dependence of the SEE, in particular the emergence of the maxima, we recall the Edelstein efficiency in an ordinary isotropic Rashba system [39]. For a single Rashba band pair, the Edelstein susceptibility scales with the band splitting in \mathbf{k} space and the modulus of the \mathbf{k} dependent in-plane spin expectation value. This relation is now transferred to the multi-band STO system. The inset in Figure 3 presents a simplified calculation based on the interplay between two competing effects: the sub-band splitting and the out-of-plane spin polarization. More specifically, to obtain this value, we take the energy-dependent average modulus of the wave vector k (or radius for circular contours) of each band and multiply it by the average modulus of the \mathbf{k} dependent in-plane spin expectation value. Next, we compute the difference between outer and inner band value of a pair. For fields higher than 180 T where the concept of ‘pairs’ is more challenging, we pair the highest energy band with the second highest energy band to form the first pair (1+2), and continue in this manner until reaching the lowest energy band (in the pair 7+8) [40]. Therefore we calculate $(k \cdot s_{\text{in-plane}})_{\text{band } i} - (k \cdot s_{\text{in-plane}})_{\text{band } i+1}$. This approach yields a result that closely resembles the efficiency calculated within the full Boltzmann approach (Figure 3), with a maximum value around 180 T. Hence, we conclude

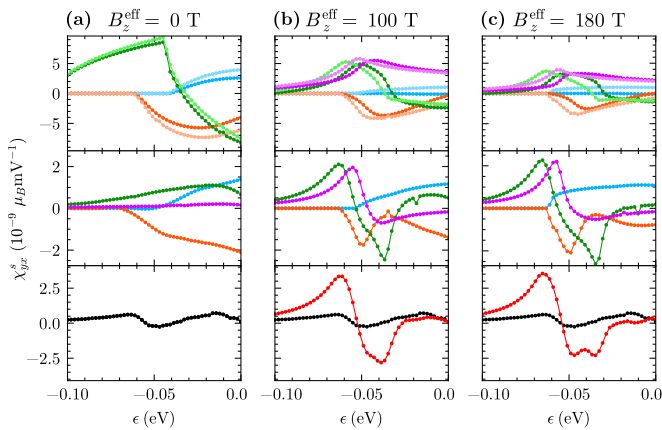


FIG. 4. Contributions to the SEE conversion efficiency at various exchange field strengths at $B_z^{\text{eff}} = 0$ T (a), $B_z^{\text{eff}} = 100$ T (b) and $B_z^{\text{eff}} = 180$ T (c). The top panel represents the efficiency of each band (with the contribution of the inner band multiplied by -1 for better comparison). The middle panel shows the efficiency contribution of each band pair. The bottom panel displays the total efficiency. The total efficiency at 0 T is represented in black.

that the SEE provided by each band pair approximately scales with $(k \cdot s_{\text{in-plane}})_{\text{band } i} - (k \cdot s_{\text{in-plane}})_{\text{band } i+1}$. In general, large sub-band splitting and large in-plane spin expectation values enhance the SEE. However, the multi-band character of the STO-based 2DEG as well as hybridization lead to a much more intricate energy dependence of the SEE compared to a trivial Rashba system, as discussed in detail in Ref. [11] for $B_z^{\text{eff}} = 0$ T.

Figure 4 provides a decomposition of the calculated SEE efficiency. In the top panel, we observe the efficiency contributed by each individual band whereas the middle panel shows the efficiency contribution of each band pair and the bottom panel displays the total efficiency.

The energy dependence of the SEE is tied to the intricate band structure at the STO interface. At zero field and low energy, the d_{xy} bands (magenta and green) exhibit notable spin-charge conversion efficiency per band (the magenta bands are above the top panel window). Nevertheless, the pair contribution remains modest, resulting in a relatively small value of χ_{yx}^s . Upon increasing the energy, the first observed extremum corresponds to the onset at -63 meV of the first d_{yz}/d_{xz} band (orange pair) with a contribution of opposite sign to χ_{yx}^s . The SEE efficiency reaches a large negative value in the region of avoided crossing points between bands of d_{xy} and d_{yz}/d_{xz} character (-50 meV to -40 meV, along the $\langle 100 \rangle$ directions). The negative maximum of the efficiency is then reached at the onset (-63 meV) of the blue band, with positive contribution.

The situation becomes more intricate in the presence of an exchange field, as the contribution of each band pair displays a less monotonic behavior, with pronounced positive and negative maxima. The general trend is however that, whereas the SEE efficiency value of each individual

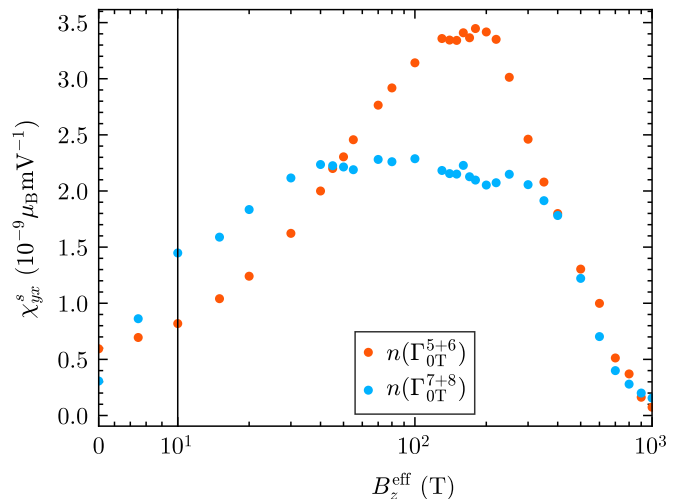


FIG. 5. Spin Edelstein effect conversion efficiency as a function of exchange field at constant charge carrier density. The SEE conversion efficiency is calculated at a fixed carrier density corresponding to the edge of the orange band (orange dots, $n = 5.44 \times 10^{13} \text{ cm}^{-2}$ at $\epsilon = -63$ meV) and the blue band (blue dots, $n = 8.99 \times 10^{13} \text{ cm}^{-2}$ at $\epsilon = -43$ meV) at 0 T, representing the positive and negative maxima of the efficiency at 0 T. The scale of the abscissa is linear from 0 T to 10 T and semi-logarithmic between 10 T and 1000 T.

band diminishes with increasing exchange field strength because of the reduced in-plane spin expectation values, excitingly, the contributions of the band pairs and the total SEE actually increase with the field up to 180 T due to Zeeman-like splitting both in energy and \mathbf{k} .

Below the onset of the orange band, the energy dependence of the SEE is not changed qualitatively by the 100 T (180 T) exchange fields. The avoided crossing between the orange and green bands occurs around -50 meV (-60 meV), whereas the avoided crossing between green and magenta band pairs is around -45 meV (-50 meV). This region eventually coincides with the onset of the lowest blue band as they are shifted by the field, altering the negative maximum.

To further illustrate the enhancement of the efficiency due to the exchange field, we present in Fig. 5 the SEE efficiency as a function of the exchange field strength, at a constant charge carrier density [41]. As explained in Figures 1 and 4, the edge of the orange band pair, which is the onset of the first heavy bands, remains unchanged in energy. Moreover, it coincides with the maximum efficiency, as observed in Figure 3. Therefore, we selected the carrier density at this energy (without exchange field; $n = 5.44 \times 10^{13} \text{ cm}^{-2}$ at $\epsilon = -63$ meV) as a reference for all field strengths.

The negative maximum of χ_{yx}^s observed around -40 meV in Figure 3 is loosely related to the edge of the blue band pair. Contrary to the orange band, its exact energy position varies with B_z^{eff} . The blue dots in Fig. 5 represent the Edelstein susceptibility for a charge carrier

density of $n = 8.99 \times 10^{13} \text{ cm}^{-2}$, which corresponds to the edge of the blue band at $B_z^{\text{eff}} = 0$ ($\epsilon = -43 \text{ meV}$).

The presence of an out-of-plane magnetic exchange field generally enhances the splitting of each band pair in terms of wave vector (k). It also tilts the spin expectation values out of the plane, thereby reducing their in-plane components. Regarding the Edelstein conversion efficiency, these two effects compete with each other, resulting in the non-monotonic behavior of the spin Edelstein effect as a function of B_z^{eff} .

For the carrier density corresponding to the edge of the orange band pair, the maximum of the curve is reached at an exchange field of 190 T. This finding aligns with the previous observations. At 180 T, as we can see in Fig. 1, the lower energy blue band is about to cross the orange bands. Slightly above this exchange field, they overlap, which modifies both the amplitude and the position of the positive maximum of the efficiency. Notably, this maximum efficiency is nearly one order of magnitude larger than the maximum efficiency without a field. On the other hand, for the blue band, it appears that we reach a plateau instead of a distinct peak. As emphasized in Figure 4, the negative maximum does not correspond to a well-defined peak.

IV. CONCLUSION

In conclusion, this study sheds light on the influence of a perpendicular exchange field on the spin-charge interconversion in the Rashba 2D electron gas at SrTiO₃ interfaces. Remarkably, increasing the magnetic field yields an up to six-fold increase of the spin-charge interconversion efficiency which we explain by the competing exchange and Rashba interactions. We have found that an out-of-plane magnetic field produces a Zeeman splitting of the band pairs thereby increasing the Edelstein effect. At the same time, it strongly modifies the Rashba-type spin textures and tilts them from their original in-plane direction towards out-of-plane thereby reducing the Edelstein effect. Therefore, a trade-off of the two competing effects causes a maximum which we observe close to a field strength of 190 T which is where shifted bands overlap close to the Γ point.

Our findings open new routes to provide more efficient SOC materials or interfaces for emerging devices such as the MESO device proposed by Intel [12]. They are also relevant because several studies have reported STO 2DEGs at interfaces with a magnetic oxide such as EuTiO₃ [17], EuO [42], or LSMO [43], with indications of induced magnetism in the 2DEG [17, 22, 43]. Finally, our results suggest a general approach that could be tested on other Rashba systems endowed with magnetic interactions, such as PdCoO₂ interface/surface states [44], EuO/KTaO₃ [45] or certain van der Waals heterostructures [46].

ACKNOWLEDGEMENT

This work received support from the ERC AdG ‘‘FRESCO’’ (#833973). I.M. acknowledges support from the DFG under SFB TRR 227.

Appendix A: Tight-binding model for STO-based 2DEGs

Following Refs. [11, 23–26], we describe the electronic states which are relevant for the formation of the 2DEG at STO interfaces by an effective tight-binding Hamiltonian \mathcal{H}_{STO} in the basis set $(d_{xy\uparrow}^{(1)}, d_{xy\uparrow}^{(2)}, d_{yz\uparrow}, d_{zx\uparrow}, d_{xy\downarrow}^{(1)}, d_{xy\downarrow}^{(2)}, d_{yz\downarrow}, d_{zx\downarrow})$. Two d_{xy} orbitals occur due to the confinement of the 2DEG along the z direction. The full Hamiltonian \mathcal{H}_{STO} can be split into three terms,

$$\mathcal{H}_{\text{STO}} = \mathcal{H}_0 + \mathcal{H}_\lambda + \mathcal{H}_{\text{OM}}. \quad (\text{A1})$$

Here, \mathcal{H}_0 is the free-electron-like Hamiltonian neglecting spin-orbit coupling,

$$\mathcal{H}_0 = \mathbb{1} \otimes \begin{pmatrix} \epsilon_{xy}^{(1)} & 0 & 0 & 0 \\ 0 & \epsilon_{xy}^{(2)} & 0 & 0 \\ 0 & 0 & \epsilon_{yz} & 0 \\ 0 & 0 & 0 & \epsilon_{zx} \end{pmatrix} \quad (\text{A2})$$

with

$$\begin{aligned} \epsilon_{xy}^{(i)} &= 2t(2 - \cos ak_x - \cos ak_y) + \epsilon_{xy0}^{(i)}, \quad i = 1, 2 \\ \epsilon_{yz} &= 2t(1 - \cos ak_y) + 2t_h(1 - \cos ak_x) + \epsilon_{z0}, \\ \epsilon_{zx} &= 2t(1 - \cos ak_x) + 2t_h(1 - \cos ak_y) + \epsilon_{z0}. \end{aligned} \quad (\text{A3})$$

Here, \mathbf{k} is the crystal momentum, a is the lattice constant, the parameters t and t_h describe nearest-neighbor hopping of the light and heavy bands, respectively, and $\epsilon_{xy0/z0}$ correspond to the on-site potentials.

The second term of the right-hand side of Eq. (A1) corresponds to atomic spin-orbit coupling,

$$\mathcal{H}_\lambda = \frac{2}{\hbar^2} \lambda \mathcal{L} \cdot \mathcal{S}, \quad (\text{A4})$$

with \mathcal{L} and \mathcal{S} the orbital angular momentum and spin operators, respectively, which are represented in our particular basis set as

$$\mathcal{L}_i = \hbar \mathbb{1} \otimes l_i, \quad i = x, y, z \quad (\text{A5})$$

with

$$\begin{aligned}
 l_x &= \begin{pmatrix} 0 & 0 & 0 & -i \\ 0 & 0 & 0 & -i \\ 0 & 0 & 0 & 0 \\ i & i & 0 & 0 \end{pmatrix}, \\
 l_y &= \begin{pmatrix} 0 & 0 & i & 0 \\ 0 & 0 & i & 0 \\ -i & -i & 0 & 0 \\ 0 & 0 & 0 & 0 \end{pmatrix}, \\
 l_z &= \begin{pmatrix} 0 & 0 & 0 & 0 \\ 0 & 0 & 0 & 0 \\ 0 & 0 & 0 & i \\ 0 & 0 & -i & 0 \end{pmatrix},
 \end{aligned} \tag{A6}$$

and

$$\mathcal{S}_i = \frac{\hbar}{2} \sigma_i \otimes \mathbf{1} \tag{A7}$$

with σ_i the Pauli spin matrices. Finally, the term \mathcal{H}_{OM} in Eq. (A1) corresponds to inter-atomic orbital mixing, arising from the broken inversion symmetry at the interface leading to a deformation of the orbitals [23, 24, 47],

$$\mathcal{H}_{\text{OM}} = \mathbf{1} \otimes \begin{pmatrix} 0 & 0 & 2ig_1 \sin ak_x & 2ig_1 \sin ak_y \\ 0 & 0 & 2ig_2 \sin ak_x & 2ig_2 \sin ak_y \\ -2ig_1 \sin ak_x & -2ig_2 \sin ak_x & 0 & 0 \\ -2ig_1 \sin ak_y & -2ig_2 \sin ak_y & 0 & 0 \end{pmatrix}. \tag{A8}$$

In this work, we use the following parameters, adopted from Refs. [11, 25],

$$\begin{aligned}
 \epsilon_{xy0}^{(1)} &= -205 \text{ meV}, & t &= 388 \text{ meV}, \\
 \epsilon_{xy0}^{(2)} &= -105 \text{ meV}, & t_h &= 31 \text{ meV}, \\
 \epsilon_{z0} &= -54 \text{ meV}, & g_1 &= 2 \text{ meV}, \\
 \lambda &= -8.3 \text{ meV}, & g_2 &= 5 \text{ meV}.
 \end{aligned} \tag{A9}$$

Appendix B: Boltzmann transport theory

Within the semiclassical Boltzmann transport theory, the current-induced magnetic moment per unit cell originating from the spin Edelstein effect is given by

$$\mathbf{m} = -\frac{A_0 g_s \mu_B}{A \hbar} \sum_{\mathbf{k}} f_{\mathbf{k}} \mathbf{S}_{\mathbf{k}}, \tag{B1}$$

with A_0 the area of the unit cell, A the area of the sample, and $f_{\mathbf{k}}$ the distribution function, which is split into an equilibrium part, the Fermi-Dirac distribution function $f_{\mathbf{k}}^0$, and a nonequilibrium part $g_{\mathbf{k}}$.

In magnetic systems, the term of Eq. (B1) containing $f_{\mathbf{k}}^0$ gives rise to an equilibrium magnetization \mathbf{m}_0 . In the

STO-based 2DEG discussed in this work, the magnetic exchange field B_{eff}^z induces a finite out-of-plane equilibrium magnetization. The application of an external electric field \mathbf{E} leads to a change of the distribution function, represented by $g_{\mathbf{k}}$, whose contribution to Eq. (B1) is a current-induced nonequilibrium magnetic moment, the Edelstein effect.

The nonequilibrium distribution function $g_{\mathbf{k}}$ is determined by solving the Boltzmann equation. Here, we consider a spatially homogeneous and stationary system,

$$\dot{\mathbf{k}} \frac{\partial f_{\mathbf{k}}}{\partial \mathbf{k}} = \left(\frac{\partial f_{\mathbf{k}}}{\partial t} \right)_{\text{scatt}}. \tag{B2}$$

In the presence of an external electric field, the semiclassical equation of motion reads

$$\dot{\mathbf{k}} = -\frac{e}{\hbar} \mathbf{E}. \tag{B3}$$

Within the relaxation time approximation, the scattering-term is expressed by

$$\left(\frac{\partial f_{\mathbf{k}}}{\partial t} \right)_{\text{scatt}} = -\frac{1}{\tau_{\mathbf{k}}} g_{\mathbf{k}} \tag{B4}$$

with $\tau_{\mathbf{k}}$ the relaxation time, which is assumed constant, $\tau_{\mathbf{k}} = \tau_0$ in our calculations.

The Boltzmann equation (B2) is then solved by

$$f_{\mathbf{k}} = f_{\mathbf{k}}^0 + \frac{\partial f_{\mathbf{k}}}{\partial \epsilon} e\tau_0 \mathbf{v}_{\mathbf{k}} \cdot \mathbf{E}. \quad (\text{B5})$$

Inserting this solution into Eq. (B1) and assuming zero temperature, Eq. (3) for the Edelstein susceptibility, characterizing the nonequilibrium current-induced magnetic moment, is obtained.

-
- [1] A. Ohtomo and H. Y. Hwang, A high-mobility electron gas at the LaAlO₃/SrTiO₃ heterointerface, *Nature* **427**, 423 (2004).
- [2] N. Reyren, S. Thiel, A. D. Caviglia, L. F. Kourkoutis, G. Hammerl, C. Richter, C. W. Schneider, T. Kopp, A.-S. Rüetschi, D. Jaccard, M. Gabay, D. A. Muller, J.-M. Triscone, and J. Mannhart, Superconducting Interfaces Between Insulating Oxides, *Science* **317**, 1196 (2007).
- [3] A. Brinkman, M. Huijben, M. van Zalk, J. Huijben, U. Zeitler, J. C. Maan, W. G. van der Wiel, G. Rijnders, D. H. A. Blank, and H. Hilgenkamp, Magnetic effects at the interface between non-magnetic oxides, *Nature Materials* **6**, 493 (2007).
- [4] L. Li, C. Richter, J. Mannhart, and R. C. Ashoori, Coexistence of magnetic order and two-dimensional superconductivity at LaAlO₃/SrTiO₃ interfaces, *Nature Physics* **7**, 762 (2011).
- [5] S. Thiel, G. Hammerl, A. Schmehl, C. W. Schneider, and J. Mannhart, Tunable Quasi-Two-Dimensional Electron Gases in Oxide Heterostructures, *Science* **313**, 1942 (2006).
- [6] A. D. Caviglia, S. Gariglio, N. Reyren, D. Jaccard, T. Schneider, M. Gabay, S. Thiel, G. Hammerl, J. Mannhart, and J.-M. Triscone, Electric field control of the LaAlO₃/SrTiO₃ interface ground state, *Nature* **456**, 624 (2008).
- [7] A. D. Caviglia, M. Gabay, S. Gariglio, N. Reyren, C. Cancellieri, and J.-M. Triscone, Tunable Rashba Spin-Orbit Interaction at Oxide Interfaces, *Physical Review Letters* **104**, 126803 (2010).
- [8] C. Cen, S. Thiel, J. Mannhart, and J. Levy, Oxide Nanoelectronics on Demand, *Science* **323**, 1026 (2009).
- [9] L. Kornblum, Conductive Oxide Interfaces for Field Effect Devices, *Advanced Materials Interfaces* **6**, 1900480 (2019).
- [10] E. Lesne, Y. Fu, S. Oyarzun, J. C. Rojas-Sánchez, D. C. Vaz, H. Naganuma, G. Sicoli, J.-P. Attané, M. Jamet, E. Jacquet, J.-M. George, A. Barthélémy, H. Jaffrès, A. Fert, M. Bibes, and L. Vila, Highly efficient and tunable spin-to-charge conversion through Rashba coupling at oxide interfaces, *Nature Materials* **15**, 1261 (2016).
- [11] D. C. Vaz, P. Noël, A. Johansson, B. Göbel, F. Y. Bruno, G. Singh, S. McKeown-Walker, F. Trier, L. M. Vicente-Arche, A. Sander, S. Valencia, P. Bruneel, M. Vivek, M. Gabay, N. Bergeal, F. Baumberger, H. Okuno, A. Barthélémy, A. Fert, L. Vila, I. Mertig, J.-P. Attané, and M. Bibes, Mapping spin-charge conversion to the band structure in a topological oxide two-dimensional electron gas, *Nature Materials* **18**, 1187 (2019).
- [12] S. Manipatruni, D. E. Nikonov, C.-C. Lin, T. A. Gosavi, H. Liu, B. Prasad, Y.-L. Huang, E. Bonturim, R. Ramesh, and I. A. Young, Scalable energy-efficient magnetoelectric spin-orbit logic, *Nature* **565**, 35 (2019).
- [13] P. Noël, F. Trier, L. M. Vicente Arche, J. Bréhin, D. C. Vaz, V. Garcia, S. Fusil, A. Barthélémy, L. Vila, M. Bibes, and J.-P. Attané, Non-volatile electric control of spin-charge conversion in a SrTiO₃ Rashba system, *Nature* **580**, 483 (2020).
- [14] J. Bréhin, F. Trier, L. M. Vicente-Arche, P. Hemme, P. Noël, M. Cosset-Chéneau, J.-P. Attané, L. Vila, A. Sander, Y. Gallais, A. Sacuto, B. Dkhil, V. Garcia, S. Fusil, A. Barthélémy, M. Cazayous, and M. Bibes, Switchable two-dimensional electron gas based on ferroelectric Ca:SrTiO₃, *Phys. Rev. Mater.* **4**, 041002 (2020).
- [15] G. M. De Luca, R. Di Capua, E. Di Gennaro, F. M. Granozio, D. Stornaiuolo, M. Salluzzo, A. Gadaleta, I. Pallecchi, D. Marrè, C. Piamonteze, M. Radovic, Z. Ristic, and S. Rusponi, Transport properties of a quasi-two-dimensional electron system formed in LaAlO₃/EuTiO₃/SrTiO₃ heterostructures, *Phys. Rev. B* **89**, 224413 (2014).
- [16] F. Gunkel, C. Bell, H. Inoue, B. Kim, A. G. Swartz, T. A. Merz, Y. Hikita, S. Harashima, H. K. Sato, M. Minohara, S. Hoffmann-Eifert, R. Dittmann, and H. Y. Hwang, Defect Control of Conventional and Anomalous Electron Transport at Complex Oxide Interfaces, *Physical Review X* **6**, 031035 (2016).
- [17] D. Stornaiuolo, C. Cantoni, G. M. De Luca, R. Di Capua, E. Di Gennaro, G. Ghiringhelli, B. Jouault, D. Marrè, D. Massarotti, F. Miletto Granozio, I. Pallecchi, C. Piamonteze, S. Rusponi, F. Tafuri, and M. Salluzzo, Tunable spin polarization and superconductivity in engineered oxide interfaces, *Nature Materials* **15**, 278 (2016).
- [18] H. R. Zhang, Y. Zhang, H. Zhang, J. Zhang, X. Shen, X. X. Guan, Y. Z. Chen, R. C. Yu, N. Pryds, Y. S. Chen, B. G. Shen, and J. R. Sun, Magnetic two-dimensional electron gas at the manganite-buffered LaAlO₃/SrTiO₃ interface, *Phys. Rev. B* **96**, 195167 (2017).
- [19] K. J. Kormondy, L. Gao, X. Li, S. Lu, A. B. Posadas, S. Shen, M. Tsoi, M. R. McCartney, D. J. Smith, J. Zhou, L. L. Lev, M.-A. Husanu, V. N. Strocov, and A. A. Demkov, Large positive linear magnetoresistance in the two-dimensional t_{2g} electron gas at the EuO/SrTiO₃ interface, *Scientific Reports* **8**, 7721 (2018).
- [20] Y. Gan, D. V. Christensen, Y. Zhang, H. Zhang, D. Krishnan, Z. Zhong, W. Niu, D. J. Carrad, K. Norrman, M. von Soosten, T. S. Jespersen, B. Shen, N. Gauquelin, J. Verbeeck, J. Sun, N. Pryds, and Y. Chen, Diluted Oxide Interfaces with Tunable Ground States, *Advanced Materials* **31**, 1805970 (2019).
- [21] R. Di Capua, M. Verma, M. Radovic, V. N. Strocov, C. Piamonteze, E. B. Guedes, N. C. Plumb, Y. Chen, M. D'Antuono, G. M. De Luca, E. Di Gennaro, D. Stornaiuolo, D. Preziosi, B. Jouault, F. Miletto Granozio, A. Sambri, R. Pentcheva, G. Ghiringhelli, and M. Salluzzo, Orbital selective switching of ferromagnetism in an oxide quasi two-dimensional electron gas, *npj Quantum Materials* **7**, 41 (2022).
- [22] J. Bréhin, Y. Chen, M. D'Antuono, S. Varotto, D. Stornaiuolo, C. Piamonteze, J. Varignon, M. Salluzzo, and

- M. Bibes, Coexistence and coupling of ferroelectricity and magnetism in an oxide two-dimensional electron gas, *Nature Physics* **19**, 823 (2023).
- [23] G. Khalsa, B. Lee, and A. H. MacDonald, Theory of t_{2g} electron-gas Rashba interactions, *Phys. Rev. B* **88**, 041302 (2013).
- [24] Z. Zhong, A. Tóth, and K. Held, Theory of spin-orbit coupling at $\text{LaAlO}_3/\text{SrTiO}_3$ interfaces and SrTiO_3 surfaces, *Phys. Rev. B* **87**, 161102 (2013).
- [25] M. Vivek, M. O. Goerbig, and M. Gabay, Topological states at the (001) surface of SrTiO_3 , *Phys. Rev. B* **95**, 165117 (2017).
- [26] A. Johansson, B. Göbel, J. Henk, M. Bibes, and I. Mertig, Spin and orbital Edelstein effects in a two-dimensional electron gas: Theory and application to SrTiO_3 interfaces, *Physical Review Research* **3**, 013275 (2021).
- [27] A. Manchon and S. Zhang, Theory of spin torque due to spin-orbit coupling, *Phys. Rev. B* **79**, 094422 (2009).
- [28] J. Krempaský, S. Muff, F. Bisti, M. Fanciulli, H. Volfová, A. P. Weber, N. Pilet, P. Warnicke, H. Ebert, J. Braun, F. Bertran, V. V. Volobuev, J. Minár, G. Springholz, J. H. Dil, and V. N. Strocov, Entanglement and manipulation of the magnetic and spin-orbit order in multiferroic Rashba semiconductors, *Nat. Commun.* **7**, 13071 (2016).
- [29] L. S. Levitov, Y. V. Nazarov, and G. M. Éliashberg, Magnetolectric effects in conductors with mirror isomer symmetry, *Sov. Phys. JETP* **61**, 133 (1985).
- [30] T. Koretsune, R. Arita, and H. Aoki, Magneto-orbital effect without spin-orbit interactions in a noncentrosymmetric zeolite-templated carbon structure, *Phys. Rev. B* **86**, 125207 (2012).
- [31] T. Yoda, T. Yokoyama, and S. Murakami, Current-induced orbital and spin magnetizations in crystals with helical structure, *Scientific Reports* **5**, 12024 (2015).
- [32] D. Go, J.-P. Hanke, P. M. Buhl, F. Freimuth, G. Bihlmayer, H.-W. Lee, Y. Mokrousov, and S. Blügel, Toward surface orbitronics: giant orbital magnetism from the orbital Rashba effect at the surface of sp -metals, *Scientific Reports* **7**, 46742 (2017).
- [33] L. Salemi, M. Berritta, A. K. Nandy, and P. M. Oppeneer, Orbitaly dominated Rashba-Edelstein effect in noncentrosymmetric antiferromagnets, *Nature Communications* **10**, 5381 (2019).
- [34] D. Hara, M. Bahramy, and S. Murakami, Current-induced orbital magnetization in systems without inversion symmetry, *Physical Review B* **102**, 184404 (2020).
- [35] J. C. Rojas Sánchez, L. Vila, G. Desfonds, S. Gambarelli, J. P. Attané, J. M. De Teresa, C. Magén, and A. Fert, Spin-to-charge conversion using Rashba coupling at the interface between non-magnetic materials, *Nat. Commun.* **4**, 2944 (2013).
- [36] J.-C. Rojas-Sánchez, S. Oyarzún, Y. Fu, A. Marty, C. Vergnaud, S. Gambarelli, L. Vila, M. Jamet, Y. Ohtsubo, A. Taleb-Ibrahimi, P. Le Fèvre, F. Bertran, N. Reyren, J.-M. George, and A. Fert, Spin to charge conversion at room temperature by spin pumping into a new type of topological insulator: α -sn films, *Phys. Rev. Lett.* **116**, 096602 (2016).
- [37] A. Dyrdał, J. Barnaś, and V. K. Dugaev, Current-induced spin polarization of a magnetized two-dimensional electron gas with Rashba spin-orbit interaction, *Phys. Rev. B* **95**, 245302 (2017).
- [38] A. Johansson, Spin-orbit driven transport: Edelstein effect and chiral anomaly, *Martin-Luther-Universität Halle-Wittenberg*, PhD thesis (2019).
- [39] V. M. Edelstein, Spin polarization of conduction electrons induced by electric current in two-dimensional asymmetric electron systems, *Solid State Communications* **73**, 233 (1990).
- [40] Note that this classification of bands affects only the approximated curve (inset) but not the accurate calculation of the Edelstein effect (main figure) based on Eq. (4).
- [41] Note that the shift of the bands caused by the exchange field alters the density of states and therefore effectively shifts the location of the Fermi energy. To compare the Edelstein signals for different field strengths it is more significant to compare configurations with equal carrier density than equal energy.
- [42] P. Lömker, T. C. Rödel, T. Gerber, F. Fortuna, E. Frantzeskakis, P. L. Fèvre, F. Bertran, M. Müller, and A. F. Santander-Syro, Two-dimensional electron system at the magnetically tunable $\text{EuO}/\text{SrTiO}_3$ interface, *Physical Review Materials* **1**, 062001(R) (2017).
- [43] W. M. Lü, S. Saha, X. R. Wang, Z. Q. Liu, K. Gopinadhan, A. Annadi, S. W. Zeng, Z. Huang, B. C. Bao, C. X. Cong, M. Venkatesan, T. Yu, J. M. D. Coey, Ariando, and T. Venkatesan, Long-range magnetic coupling across a polar insulating layer, *Nature Communications* **7**, 11015 (2016).
- [44] J. H. Lee, T. Harada, F. Trier, L. Marcano, F. Godel, S. Valencia, A. Tsukazaki, and M. Bibes, Nonreciprocal Transport in a Rashba Ferromagnet, Delafossite PdCoO_2 , *Nano Letters* **21**, 8687 (2021).
- [45] H. Zhang, Y. Yun, X. Zhang, H. Zhang, Y. Ma, X. Yan, F. Wang, G. Li, R. Li, T. Khan, Y. Chen, W. Liu, F. Hu, B. Liu, B. Shen, W. Han, and J. Sun, High-Mobility Spin-Polarized Two-Dimensional Electron Gases at $\text{EuO} / \text{KTaO}_3$ Interfaces, *Physical Review Letters* **121**, 116803 (2018).
- [46] S. Shi, X. Wang, Y. Zhao, and W. Zhao, Recent progress in strong spin-orbit coupling van der Waals materials and their heterostructures for spintronic applications, *Materials Today Electronics* **6**, 100060 (2023).
- [47] L. Petersen and P. Hedegård, A simple tight-binding model of spin-orbit splitting of sp -derived surface states, *Surface Science* **459**, 49 (2000).